



Three-dimensional stable lithium metal anode with nanoscale lithium islands embedded in ionically conductive solid matrix

Dingchang Lin^a, Jie Zhao^a, Jie Sun^a, Hongbin Yao^a, Yayuan Liu^a, Kai Yan^a, and Yi Cui^{a,b,1}

^aDepartment of Materials Science and Engineering, Stanford University, Stanford, CA 94305; and ^bStanford Institute for Materials and Energy Sciences, SLAC National Accelerator Laboratory, Menlo Park, CA 94025

Edited by Thomas E. Mallouk, The Pennsylvania State University, University Park, PA, and approved March 23, 2017 (received for review November 25, 2016)

Rechargeable batteries based on lithium (Li) metal chemistry are attractive for next-generation electrochemical energy storage. Nevertheless, excessive dendrite growth, infinite relative dimension change, severe side reactions, and limited power output severely impede their practical applications. Although exciting progress has been made to solve parts of the above issues, a versatile solution is still absent. Here, a Li-ion conductive framework was developed as a stable “host” and efficient surface protection to address the multi-faceted problems, which is a significant step forward compared with previous host concepts. This was fulfilled by reacting overstoichiometry of Li with SiO. The as-formed Li_xSi-Li₂O matrix would not only enable constant electrode-level volume, but also protect the embedded Li from direct exposure to electrolyte. Because uniform Li nucleation and deposition can be fulfilled owing to the high-density active Li domains, the as-obtained nanocomposite electrode exhibits low polarization, stable cycling, and high-power output (up to 10 mA/cm²) even in carbonate electrolytes. The Li-S prototype cells further exhibited highly improved capacity retention under high-power operation (~600 mAh/g at 6.69 mA/cm²). The all-around improvement on electrochemical performance sheds light on the effectiveness of the design principle for developing safe and stable Li metal anodes.

Li metal | 3D composite | electrolyte proof | overlithiation | high-power output

Extensive research has been conducted on developing advanced lithium (Li) battery anode substitutes, including silicon (1–5), tin (6, 7), and Li metal (8–15), for high-energy applications in portable electronics and electrical transportation. Among all, Li metal is recognized as the most attractive candidate, where its lowest electrochemical potential (Li⁺/Li = −3.040 V vs. standard hydrogen electrode) and highest theoretical specific capacity (3,860 mAh/g) have attracted broad scientific and technological interest (16–18). Despite continuous efforts on Li metal, its practical application has remained stagnant due to many materials challenges. The root causes lie in two aspects: the high chemical reactivity of Li metal and significant dimensional change during charge/discharge, which together generate other observed problems including solid electrolyte interphase (SEI) fracture and dendritic deposition.

Since the advent of Li batteries, great progress has been made in understanding Li metal plating/stripping behavior (8, 9, 12, 19, 20), preventing Li dendrite formation and penetration (13, 21–25), as well as improving Coulombic efficiency (CE) (14, 26, 27). Although further improvement in ionic conductivity and interfacial contact is still required, solid electrolytes were proven to be efficacious for mitigating dendrite penetration (22, 23, 28–33). Developing electrolyte additives is also effective in stabilizing SEI and homogenizing Li deposition (13, 26, 27, 34), whereas engineering chemically and mechanically stable interfacial layer is also a prominent alternative to stabilize SEI (14). Although the high reactivity of Li metal has received sufficient attention, the studies were based on dense Li foil, which imposed grand challenges by introducing large dimensional change.

We recently proposed that volume variation is one of the two root causes attracting much recent attention. In contrast to a carbonaceous anode with ~10% volume change during cycling, “hostless” Li foil in principle exhibits infinite relative volume change during the stripping/plating cycle (35–37). On one hand, the enormous volume change generates engineering challenges at the cell level by introducing internal stress. On the other hand, SEI is vulnerable to the moving interface and prone to fracture (19, 38, 39). Continuous SEI formation during cycling would not only decompose electrolyte and consume Li ion but also accumulate an ionic insulating layer which further blocks the ion transport (40). Moreover, dendritic and mossy Li arises from uneven Li-ion flux might penetrate through the separator and cause an internal short circuit, triggering the danger of thermal runaway and explosion hazards (18). During the stripping process, dendritic morphology can aggravate the formation of dead Li and thus result in low CE (9, 41). Moreover, due to the limited accessible active surface of planar Li foil, practical power operation (5–10 mA/cm² of current density) with Li metal anodes is not possible at present (16).

To address these issues, a new direction was recently developed based on the concept of constructing a 3D stable host to store Li metal, which was realized with graphene oxide (35), nanofiber matrix (36, 37), and hollow carbon spheres (42). The as-obtained composite electrodes afford minimized volume change to less than 20% and thus more stable SEI. In addition, by creating a large surface in contact with liquid electrolytes, ion flux can be homogenized so that high-power and dendrite-free operation can be achieved. With the remarkable improvement in performance demonstrated by these examples, we believe that a

Significance

Lithium metal anode holds great promises for next-generation high-energy lithium battery systems. This work introduces an electrolyte-proof design of three-dimensional lithium metal anode where most of the lithium domains are embedded in a lithium-ion conductive matrix. In this architecture, the lithium-ion conductive matrix can isolate the embedded lithium domains from liquid electrolyte and thus prevent severe initial side reactions, while the matrix can simultaneously transport lithium ion and maintain the electrochemical activity of the embedded lithium. The design principle enables highly stable, high-power, and safe lithium metal anodes with minimal side reactions and negligible volume variation during cycling, which paves the way for viable lithium metal batteries in the future.

Author contributions: D.L. and Y.C. designed research; D.L., J.Z., J.S., H.Y., and Y.L. performed research; D.L. and J.Z. contributed new reagents/analytic tools; D.L., K.Y., and Y.C. analyzed data; and D.L. and Y.C. wrote the paper.

The authors declare no conflict of interest.

This article is a PNAS Direct Submission.

¹To whom correspondence should be addressed. Email: yicui@stanford.edu.

This article contains supporting information online at www.pnas.org/lookup/suppl/doi:10.1073/pnas.1619489114/-DCSupplemental.

significant step forward is to construct a Li-ion conductive stable host as matrix with embedded Li metal to form the 3D anode. Rather than having high-surface Li in direct contact with liquid electrolyte, which would generate more SEI at the early stage, embedding Li domains inside a Li-ion conducting matrix would protect the highly reactive Li from excess side reactions at the early stage, while simultaneously guaranteeing the electrochemical activity of the Li. We would expect such a concept to hold not only the merits of previous 3D anodes, but also to provide a preengineered Li surface protection to alleviate the initial side reactions.

Herein, we developed a facile chemical synthesis method to realize such a Li-ion conductive nanocomposite electrode (LCNE). By having SiO reacted with an overstoichiometric amount of Li, we are able to obtain a $\text{Li}_x\text{Si}-\text{Li}_2\text{O}$ matrix with embedded Li domains, where the matrix can conduct Li ion and protect the metallic Li. With the structure, a negligible volume change, reduced initial side reactions, and stable high-current operation up to $10 \text{ mA}/\text{cm}^2$ can be simultaneously obtained where the performance parameters are unprecedented. In addition, a highly improved rate capability in Li-S prototype cells was further demonstrated. We believe the design principle in 3D Li architecture will offer exciting opportunities for developing stable Li metal anode and pave the way for the next-generation high-energy Li batteries.

Results and Discussion

Stable Electrode Dimension and Dendritic Suppression. Fig. 1A schematically shows the open-framework architecture of 3D Li with stable host that was used previously by most of the works (35–37), where Li was coated onto a scaffold that serves as the stable host. Under this circumstance, Li would be exposed directly to the liquid electrolytes in a cell, which would further bring about severe side reactions at the initial stage. Despite the fact that SEI can be stabilized in the later cycles by minimized dimensional change and more uniform deposition, excess initial SEI formation is still

undesired. A better alternative to this design is an electrolyte-proof embedded Li as shown in Fig. 1B. In this design, Li-ion conductive materials are exploited to construct the host, whereas most of the Li domains are embedded in the matrix without direct contact with liquid electrolytes. Nevertheless, because of the Li-ion conduction capability of the matrix, the embedded Li domains are still electrochemically active. As a consequence, the merits of 3D Li would still hold whereas initial side reactions would be highly reduced.

Our synthetic strategy on the abovementioned structure is to use overstoichiometric reaction of Li with SiO or “overlithiation” of SiO, extended from stoichiometric prelithiation with molten Li (43). In conventional prelithiation studies, stoichiometric amount of molten Li metal was used to chemically convert Si, SiO_x , metal oxides, and fluorides into Li_xSi , Li_2O , LiF (43–46), and there is no extra Li metal in the final products. Here, an extra amount of Li was intentionally added into SiO, where porous $\text{Li}_x\text{Si} + \text{Li}_2\text{O}$ was first obtained as a matrix and followed by the intake of molten Li to the pores.

By screening multiple compounds, it was found that the overlithiation behavior of metastable SiO phase is rather unique. Violent reaction was observed when the overstoichiometric amount of molten Li and submicrometer-sized SiO powder (*SI Appendix*, Fig. S1) were mixed at elevated temperature of $\sim 300^\circ\text{C}$. It was noted that nanoporous $\text{Li}_x\text{Si}-\text{Li}_2\text{O}$ composite was obtained in the form of a matrix under vigorous stirring, where Li_xSi and Li_2O can serve as the Li-ion conductive components (47), with the extra amount of Li embedded within the nanopores. As the reaction is complete, dry silvery powders (*SI Appendix*, Fig. S2) were obtained even above the melting temperature of Li, indicating full infusion of metallic Li into the nanopores of the matrix. The size of the powder particles is on the order of tens or hundreds of micrometers, much larger than the dimension ($\sim 100 \text{ nm}$) previously demonstrated in the open-framework architectures (36, 37). This significantly reduces the exposure of Li and the initial formation of SEI on the

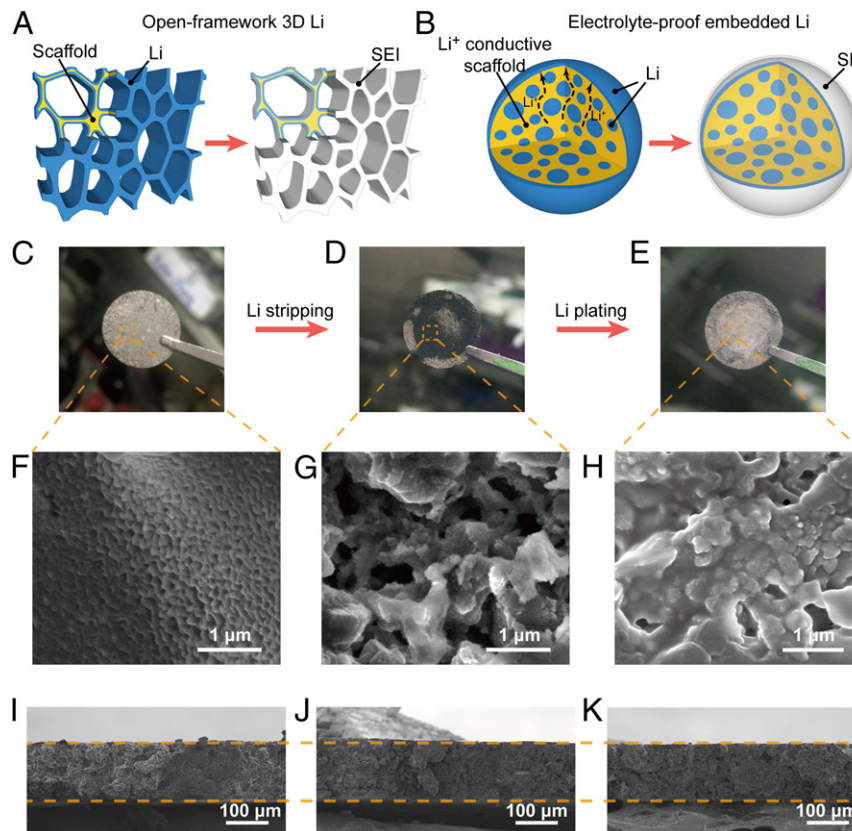


Fig. 1. Synthetic procedures and stripping/plating behavior of as-obtained electrode. (A) Schematic showing the open-framework configuration of Li metal anode with stable host, where the scaffold is coated by metallic Li. In this case, Li metal faces directly with the liquid electrolyte, which brings about excess SEI formation at the early stage. (B) Schematic illustration of the electrolyte-proof configuration where the majority of Li is embedded in a Li-ion conductive scaffold. After immersing into electrolytes, SEI only forms on the outer surface while the embedded Li domains remain intact. (C–H) Digital photo images (C–E) and corresponding SEM images (F–H) showing the pristine (C and F) LCNE after stripping $8 \text{ mAh}/\text{cm}^2$ (D and G) and LCNE after plating $8 \text{ mAh}/\text{cm}^2$ of Li back (E and H). (I–K) Cross-section SEM images of pristine LCNE (I), LCNE after stripping $8 \text{ mAh}/\text{cm}^2$ of Li (J), and electrode after stripping and plating back $8 \text{ mAh}/\text{cm}^2$ of Li (K). The current density was set at $2 \text{ mA}/\text{cm}^2$ for all of the above characterizations.

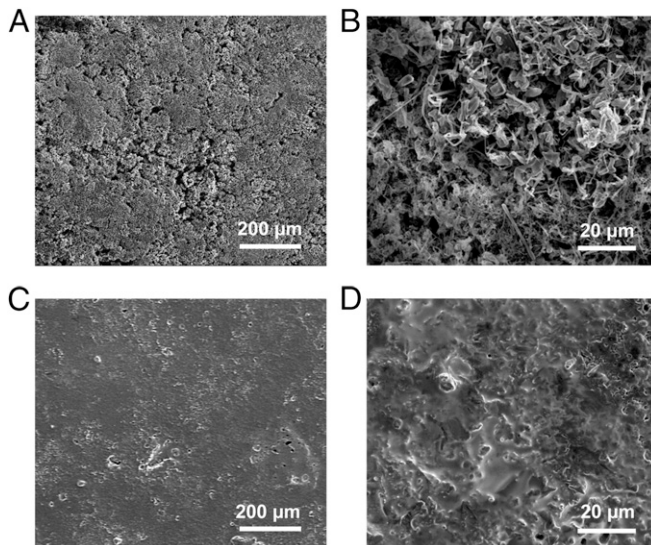


Fig. 2. Characterization on morphology of Li deposited on different Li metal electrodes after 20 cycles. (*A* and *B*) Low-magnification (*A*) and magnified (*B*) SEM images showing the Li deposition behavior on Li foil (*B*) after 20 cycles. (*C* and *D*) Low-magnification (*C*) and magnified (*D*) SEM images showing the Li deposition behavior on LCNE after 20 cycles. The current density was fixed at 1 mA/cm² for both Li stripping and plating processes. The stripping/plating capacity was 1 mAh/cm².

particle surfaces. Subsequently, the LCNEs were obtained by applying a mechanical press on the powders to afford the pellet electrodes (*SI Appendix*, Fig. S3). The thickness of the LCNEs can be varied by controlling the amount of powder for a certain pressing area. (*SI Appendix*, Fig. S4).

Fig. 1*C* shows the digital photo of an as-obtained LCNE, which exhibits silvery color with a flat surface. The corresponding magnified scanning electron microscopy (SEM) image indicates uniform surface coverage by nanosized domains of metallic Li (Fig. 1*F*), which accounts for the observed color. To study the internal porous structure of the matrix, 8 mAh/cm² of Li (~50% of Li metal capacity) was stripped from the electrode through galvanostatic charging. After Li stripping, the top surface of the electrode exhibited obvious silvery-to-black color change (Fig. 1*D*), where the black color may be originated from Li_xSi as well as the optical antireflection effect of the nanoporous structure. From the SEM image (Fig. 1*G*) of the delithiated electrode, submicrometer- and nanosized pores, which were initially occupied by Li, were clearly visualized. The domain size of the matrix is hundreds of nanometers. Afterward, when the 8 mAh/cm² of Li was plated back, the silvery color recovered as observed from Fig. 1*E*. The corresponding surface characterization further showed that almost all of the pores were refilled by Li without obvious Li dendrites (Fig. 1*H*).

Electrode thickness variation was also characterized by ex situ SEM study to examine the electrode-level dimension stability after Li stripping/plating. The thickness of LCNEs under three conditions, including pristine (Fig. 1*I*), half-striped (8 mAh/cm², Fig. 1*J*), and after one stripping/plating cycle (Fig. 1*K*), was measured and compared. To guarantee that each condition had the same initial thickness, the electrodes of the three conditions came from the same original piece, where an LCNE was equally cut into individual segments for each condition. As shown in Fig. 1 *I–K*, the three conditions exhibited almost identical thickness of ~138 μm, which demonstrates a near-constant electrode dimension during stripping/plating processes with the Li-ion conductive matrix as the host.

To compare the surface morphology of Li foil and LCNEs after cycling, SEM characterization was conducted after 20 galvanostatic cycles at a current density of 1 mA/cm² and a capacity of 1 mAh/cm². The low-magnification and magnified SEM images of the Li foil surface after cycling are shown in Fig. 2 *A* and *B*, respectively. From the low-magnification image, high roughness can be observed, with excessive growth of dendritic Li on the whole surface. This was further confirmed by the magnified SEM image, where loosely stacked Li dendrites and nanofilaments were observed. In contrast, the surface of LCNE after 20 cycles (Fig. 2*C*) remained consistently flat over a large area. The high-resolution image further indicates more uniform Li deposition (Fig. 2*D*). Such stark contrast strongly supports that the LCNE is capable of maintaining stable structure and suppressing dendrite evolution through continuous cycling.

The above experiments all support the uniform Li deposition within the matrix, which can be attributed to the Li-ion conductive nature and thus highly increased active surface of the matrix. For Li foil, only the very top surface can have access to Li ion. As a result, the local ion flux would be too concentrated to enable uniform Li deposition. In contrast, with Li-ion conductive matrix, Li ion can also be transported into the bulk without excessive exposure to liquid, which activates many more Li nucleation sites and reduces side reactions. In addition, with a highly increased number of Li nuclei for further deposition, uneven deposition and thus dendritic growth can also be suppressed.

It is noted that the composites still retain high specific capacity. As shown in *SI Appendix*, Fig. S5*A*, when the electrode was delithiated to 1 V vs. Li⁺/Li, ~2,250 mAh/g could be extracted (based on the total electrode weight), where Li metal contributed ~1,300 mAh/g. The phases at different delithiation stages were confirmed by X-ray diffraction in *SI Appendix*, Fig. S5*B*, where no Li signal could be observed at stage B (0.15-V cutoff). After the electrode was fully delithiated to 1 V, the structure of the whole electrode could still be maintained (*SI Appendix*, Fig. S6), which demonstrated the dimensional stability and interconnected nature of the matrix.

Fewer Initial Side Reactions and Stable Li Stripping/Plating. To study the electrochemical behavior of the LCNEs, symmetric cells with LCNEs as both electrodes were tested in carbonate electrolyte. Electrochemical impedance spectroscopy (EIS) was first exploited prior to battery cycling to evaluate the initial SEI formation. It is noted that the semicircle obtained at high frequency in this cell configuration can be attributed to the SEI and charge-transfer resistance. Once SEI keeps accumulating over time, augmentation in the resistance can be expected accordingly. Fig. 3*A* shows the Nyquist plots of an LCNE symmetric cell in the first 12 h. It was observed that the resistance was almost constant through the first 12 h, indicating the prompt passivation of surface by SEI at the initial stage without excess side reactions. In contrast, the resistance of a symmetric cell based on the previously reported layered Li-reduced graphene oxide (rGO) increased gradually in the same time frame (Fig. 3*B*), which can be attributed to the high exposure of Li and thus more initial side reactions. In addition, it was found that the resistance of the LCNE symmetric cell is significantly lower than that of the layered Li-rGO counterpart, which indicates that LCNE affords an even larger active Li surface. These facts strongly support that the Li-ion conductive matrix can efficiently isolate the embedded Li from liquid electrolyte and still maintain its electrochemical activity.

The first galvanostatic cycle of both LCNEs and Li foil electrodes was further analyzed. As shown in Fig. 3*C*, large overpotential was observed for Li foil cells during the initial charging (I, ~400 mV), followed by a gradual drop in overpotential (gradual decline to ~100 mV) in the later stage. During discharging, overpotential “bump” was initially shown (II), followed by a plateau with a relatively low overpotential and later discharge overpotential augmentation

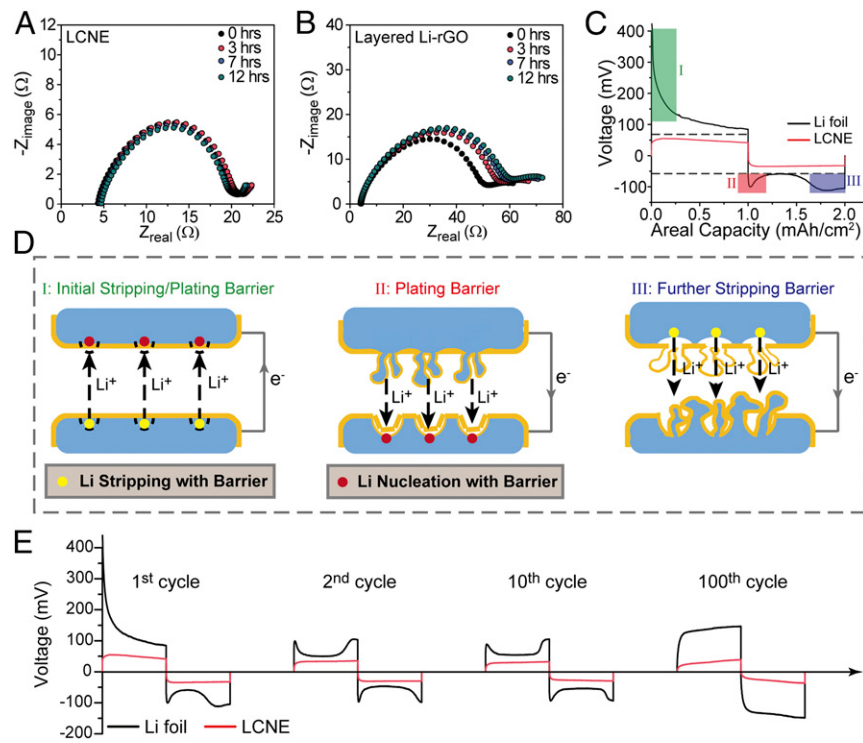


Fig. 3. Electrochemical characteristics of Li stripping/plating and their mechanisms. (A and B) Time-dependent Nyquist plots showing the impedance evolution of symmetric cells with LCNE (A) and Li foil (B) electrodes. (C) Typical stripping/plating voltage profile of the Li foil (black) and LCNE (red) of the first galvanostatic cycle. (D) Schematic shows the initial stripping/plating barrier (corresponding to barrier I in C), plating barrier (corresponding to barrier II in C), and further stripping barrier (corresponding to barrier III in C). (E) Voltage profile of Li foil symmetric cell (black) and LCNE symmetric cell (red) at the 1st, 2nd, 10th, and 100th cycle. The current density and the areal capacity were fixed at $1 \text{ mA}/\text{cm}^2$ and $1 \text{ mAh}/\text{cm}^2$, respectively.

(III). Fig. 3D schematically shows the mechanisms of the Li stripping/plating behaviors corresponding to the regions I, II, and III in Fig. 3C. The origins of the energy barriers at each stage were marked as yellow (stripping barrier) and red (nucleation barrier) dots on the electrode surface. For the as-assembled cells, the relatively thick native oxide layer and spontaneously formed SEI can block ion transport, which would not only hinder the Li stripping from the bottom electrode, but also hamper the Li deposition on the top, both contributing to the much higher overpotential (region I). At the discharge stage, the freshly deposited Li on the top electrode is rather easy to strip due to the thin as-formed SEI layer. However, the concave surface of the bottom electrode covered by thick SEI requires a high-energy barrier for Li nucleation, contributing to the higher overpotential in region II. Afterward, newly grown Li would facilitate further deposition, which reduces the overpotential as shown between regions II and III. Once the Li freshly deposited from the last charging onto the top electrode is exhausted, stripping from original top Li foil beneath the thick SEI is required. This imposes higher energy barrier and leads to the final overpotential augmentation (III).

In contrast, the LCNE symmetric cells showed flat plateaus as well as much lower overpotential at the charging/discharging stages, without an obvious “bump” during cycling. This indicates a lower-energy barrier for both its nucleation and stripping processes. With continuous Li-ion conductive matrix, high-surface-active Li can serve as a nucleus, enabling 3D Li plating/stripping, which contributes to the observed low-energy barrier. EIS measurements further support the above statements, where LCNE cells exhibited constant low resistance initially and after 10 cycles (*SI Appendix*, Fig. S11). In contrast, the Li foil cells showed large resistance ($\sim 650 \Omega/\text{cm}^2$) before cycling, followed by highly reduced resistance ($\sim 85 \Omega/\text{cm}^2$) after 10 cycles as a result of native oxide collapse and dendritic Li formation. In addition, consistently low overpotential and flat voltage plateaus can be maintained for the LCNE cells for prolonged cycles (Fig. 3E). In contrast, the Li foil cells exhibited gradual increase in overpotential through the cycling, which can be attributed to the accumulation of thick SEI and the continuous consumption of electrolyte by the side reactions.

The LCNE cell also exhibits outstanding rate capability and cycling stability at different current density. As shown in Fig. 4A, where the current density is varied from 0.5 to $5 \text{ mA}/\text{cm}^2$, low overpotential from $\sim 18 \text{ mV}$ (at $0.5 \text{ mA}/\text{cm}^2$) to $\sim 100 \text{ mV}$ (at $5 \text{ mA}/\text{cm}^2$) can be obtained for LCNEs, much lower than those of the Li foil counterparts. The cycling stability at current density of $1\text{--}10 \text{ mA}/\text{cm}^2$ was further demonstrated (Fig. 4B). At $1 \text{ mA}/\text{cm}^2$ (Fig. 4B, Top), stable cycling with low overpotential of $\sim 32 \text{ mV}$ and flat voltage plateaus was observed through 100 cycles, whereas the Li foil cells showed continuous increase in overpotential from ~ 65 to $\sim 140 \text{ mV}$. In prolonged cycles, the LCNEs still exhibited stable cycling with minimal overpotential increase, whereas the Li foils suffered internal short circuit after ~ 160 cycles (*SI Appendix*, Fig. S12). The cycling stability of the LCNEs and the Li foil electrodes diverged even more at further increased current densities of $3 \text{ mA}/\text{cm}^2$ (*SI Appendix*, Fig. S13), $5 \text{ mA}/\text{cm}^2$ (Fig. 4B, Middle), and $10 \text{ mA}/\text{cm}^2$ (Fig. 4B, Bottom), where LCNE continued to afford stable cycling with low overpotential but the Li foil counterparts showed a dramatic overpotential increase over cycles. It is noted that the overpotential of Li foil electrodes started to decrease and fluctuate after tens of cycles, which can be attributed to the internal soft short circuit by Li dendrite propagation. When the cells were cycled at a higher areal capacity of $3 \text{ mAh}/\text{cm}^2$ (*SI Appendix*, Fig. S14), the LCNEs can still maintain good stability with low overpotential, whereas the Li foil counterparts exhibited a dramatic overpotential increase followed by internal short circuit after tens of cycles.

The cycle life of Li metal anodes paired with high-areal-capacity $\text{Li}_4\text{Ti}_5\text{O}_{12}$ (LTO) can be a good indicator of the Coulombic efficiency of Li anodes with extra prestored Li (35, 36). Here, the LCNEs with areal capacity of $\sim 12 \text{ mAh}/\text{cm}^2$ were paired with LTO ($\sim 3 \text{ mAh}/\text{cm}^2$), which shows stable cycling without significant decay for at least 90 cycles, outperforming both the Li foil and electrodeposited Li on Cu (*SI Appendix*, Fig. S16).

The cycling test at various current densities was further carried out in ether-based electrolyte. Ether-based electrolyte is generally known to be a much better electrolyte for Li metal anodes because more flexible SEI layer can form to accommodate the surface

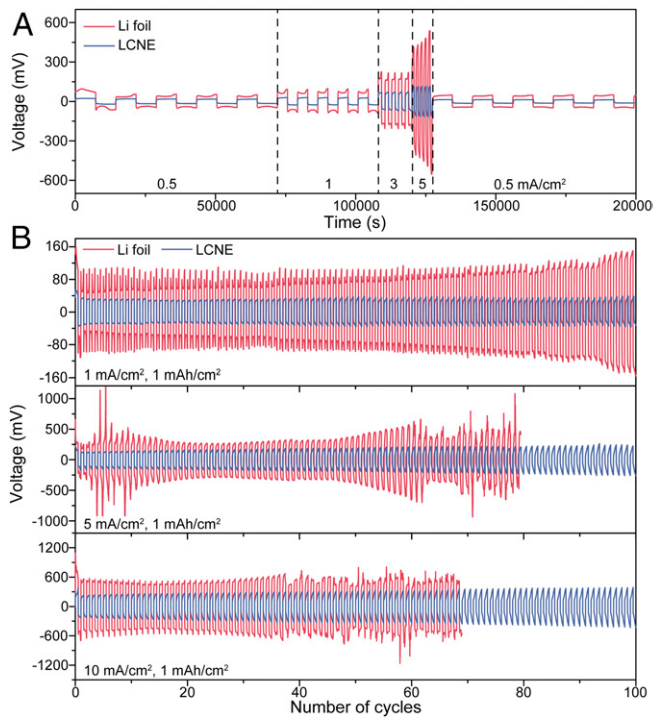


Fig. 4. Electrochemical performance of LCNE symmetric cell. (A) Voltage profile of Li foil symmetric cell (red) and that of LCNE symmetric cell (blue) at different rate various from 0.5 to $5\text{ mA}/\text{cm}^2$. (B) The voltage profiles of Li foil symmetric cells (red) and LCNE symmetric cells (blue) at various current densities of $1\text{ mA}/\text{cm}^2$ (Top), $5\text{ mA}/\text{cm}^2$ (Middle), and $10\text{ mA}/\text{cm}^2$ (Bottom). Stripping/plating capacity is fixed at $1\text{ mAh}/\text{cm}^2$.

fluctuation during stripping/plating (48). As a result, much more uniform Li deposition can already be achieved with Li foil. Nevertheless, the LCNEs can still outperform the Li foils in an ether-based system. As shown in *SI Appendix*, Fig. S17A, at a current density of $1\text{ mA}/\text{cm}^2$ the Li foil electrode showed high overpotential in the early cycles followed by a gradual decrease. This decreasing phenomenon can be attributed to the dendritic Li growth, which

significantly increases the surface area (20). For LCNE cells, a constantly lower overpotential of $\sim 15\text{ mV}$ can be obtained throughout the whole 100 cycles. At a high current density of $5\text{ mA}/\text{cm}^2$ (*SI Appendix*, Fig. S17B), LCNEs also exhibited stable cycling while the Li foil counterpart showed obvious voltage fluctuation.

Improved Rate Capability of Li-S Batteries. Metallic Li is prominent for Li-S battery systems (16, 49, 50). With the low-energy barrier and stable LCNE as anodes, we further demonstrated their electrochemical performance in Li-S batteries. Here, $12.5\text{ }\mu\text{L}/\text{cm}^2$ $5\text{ M Li}_2\text{S}_8$ in 1:1 vol/vol 1,3-dioxolane (DOL)/1,2-dimethoxyethane (DME) ($2\text{-mg}/\text{cm}^2$ equivalent mass loading of S) was loaded on KOH-treated electrospun carbon nanofibers as the cathodes. A rate capability test with current densities varied from 0.2 to 2 C was carried out (based on theoretical capacity of S $1,673\text{ mAh/g}$, $1\text{ C} = 3.34\text{ mA}/\text{cm}^2$). Fig. 5 shows the notable rate capability differences between Li-S cells with LCNEs and Li foils as the anodes. At the early stage with low current density, a high capacity of $\sim 1,000\text{ mAh/g}$ can be retained for both anodes. However, it is clearly shown in Fig. 5 A and B that the LCNE-S cells exhibited lower overpotential compared with the Li foil counterpart. A more pronounced difference appeared when the current density was further increased. At 2 C , which is equivalent to $6.69\text{ mA}/\text{cm}^2$, the Li foil-S cell lost its second plateau ($\text{Li}_2\text{S}_6 \rightarrow \text{Li}_2\text{S}$) with cutoff voltage at 1.7 V , which gave rise to a significant capacity drop. In contrast, the LCNE-S cell yielded much better kinetics, with a second plateau of $\sim 1.9\text{ V}$ even at the high rate of 2 C . Fig. 5C clearly shows the capacity retention at different C rates during cycling. For the LCNE-S cell, $\sim 1,050\text{ mAh/g}$ of specific capacity can be obtained at 0.2 C , whereas at 10-fold higher current density (2 C), the capacity still remained over 600 mAh/g . In contrast, much lower specific capacity retention was observed for the Li foil-S cell especially at high rate as the capacity dropped significantly from $\sim 950\text{ mAh/g}$ at 0.2 C to less than 100 mAh/g at 2 C .

Conclusions

This work demonstrated a Li-ion conductive matrix as the “host” and surface protection for Li metal anodes to address the active surface versus side reaction dilemma, which was fulfilled by the overlithiation of SiO to yield Li-embedded $\text{Li}_x\text{Si}-\text{Li}_2\text{O}$ matrix as the stable electrode (LCNE). The as-obtained LCNE proves highly reduced initial side reactions compared with the previously reported “open-framework” architecture, while constant electrode-level

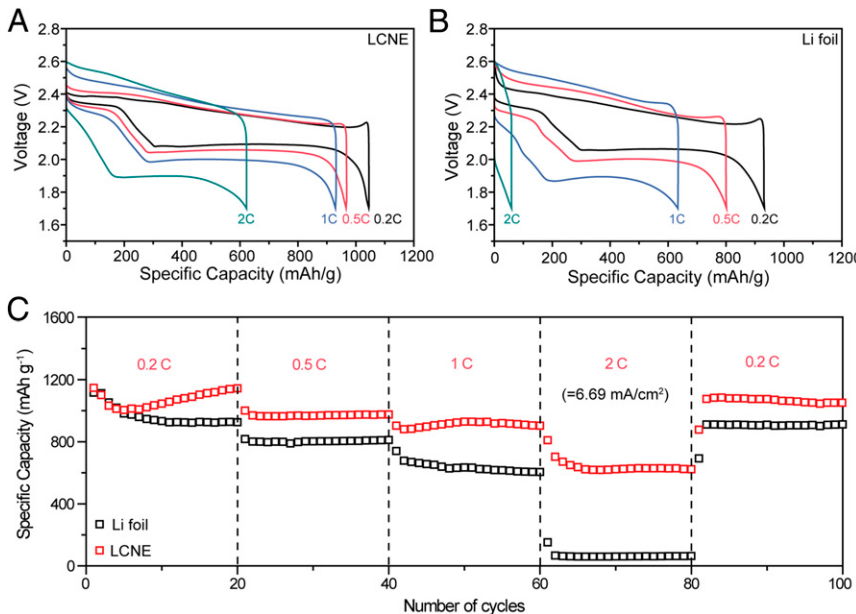


Fig. 5. Rate capability of Li-S batteries with different Li electrodes. (A and B) Voltage profile of Li-S batteries with LCNE (A) and Li foil (B) as negative electrodes. Mass loading of S is fixed at $2\text{ mg}/\text{cm}^2$. C rate is various from 0.2 to 2 C ($6.69\text{ mA}/\text{cm}^2$). (C) Capacity retention of Li-S batteries at different C rate with LCNE (red) and Li foil (black) as negative electrodes.

dimension and further homogenized Li deposition were obtained. Although Li was well protected, a larger active surface with even lower impedance was fulfilled by the Li-ion conductive network, rendering low polarization and stable cycling with flat plateaus. This further contributes to the excellent cycling stability with much lower polarization at various current densities up to 10 mA/cm^2 for at least 100 cycles, whereas a similar effect was also attained in an ether-based electrolyte system. By integrating LCNEs into Li-S batteries, highly improved rate capability especially at high current density can be observed. This work creates a design principle as well as material synthesis strategy for Li metal anode and opens up

exciting opportunities for the next-generation high-energy, power-intensive Li metal batteries under safe and stable operation.

Materials and Methods

Materials and methods, including overlithiation of SiO, LCNE fabrication, characterizations, electrochemical measurements on symmetric cells, lithium polysulphide (Li_2S_8) solution preparation, and Li-S batteries tests can be found in *SI Appendix*.

ACKNOWLEDGMENTS. Y.C. acknowledges the support from the Assistant Secretary for Energy Efficiency and Renewable Energy, Office of Vehicle Technologies of the US Department of Energy under the Battery Materials Research Program and Battery500 Consortium.

1. Chan CK, et al. (2008) High-performance lithium battery anodes using silicon nanowires. *Nat Nanotechnol* 3:31–35.
2. Magasinski A, et al. (2010) High-performance lithium-ion anodes using a hierarchical bottom-up approach. *Nat Mater* 9:353–358.
3. Wu H, et al. (2012) Stable cycling of double-walled silicon nanotube battery anodes through solid-electrolyte interphase control. *Nat Nanotechnol* 7:310–315.
4. Liu N, et al. (2014) A pomegranate-inspired nanoscale design for large-volume-change lithium battery anodes. *Nat Nanotechnol* 9:187–192.
5. Lin D, et al. (2015) A high tap density secondary silicon particle anode fabricated by scalable mechanical pressing for lithium-ion batteries. *Energy Environ Sci* 8:2371–2376.
6. Yang J, Winter M, Besenhard JO (1996) Small particle size multiphase Li-alloy anodes for lithium-ion batteries. *Solid State Ion* 90:281–287.
7. Whitehead AH, Elliott JM, Owen JR (1999) Nanostructured tin for use as a negative electrode material in Li-ion batteries. *J Power Sources* 81–82:33–38.
8. Peled E (1979) The electrochemical behavior of alkali and alkaline earth metals in nonaqueous battery systems—the solid electrolyte interphase model. *J Electrochem Soc* 126:2047–2051.
9. Yamaki J-i, et al. (1998) A consideration of the morphology of electrochemically deposited lithium in an organic electrolyte. *J Power Sources* 74:219–227.
10. Bhattacharya R, et al. (2010) In situ NMR observation of the formation of metallic lithium microstructures in lithium batteries. *Nat Mater* 9:504–510.
11. Chandrashekhar S, et al. (2012) ${}^7\text{Li}$ MRI of Li batteries reveals location of microstructural lithium. *Nat Mater* 11:311–315.
12. Harry KJ, Hallinan DT, Parkinson DY, MacDowell AA, Balsara NP (2014) Detection of subsurface structures underneath dendrites formed on cycled lithium metal electrodes. *Nat Mater* 13:69–73.
13. Ding F, et al. (2013) Dendrite-free lithium deposition via self-healing electrostatic shield mechanism. *J Am Chem Soc* 135:4450–4456.
14. Zheng G, et al. (2014) Interconnected hollow carbon nanospheres for stable lithium metal anodes. *Nat Nanotechnol* 9:618–623.
15. Lu Y, Tu Z, Archer LA (2014) Stable lithium electrodeposition in liquid and nanoporous solid electrolytes. *Nat Mater* 13:961–969.
16. Bruce PG, Freunberger SA, Hardwick LJ, Tarascon JM (2011) Li-O₂ and Li-S batteries with high energy storage. *Nat Mater* 11:19–29.
17. Lin D, Liu Y, Cui Y (2017) Reviving the lithium metal anode for high-energy batteries. *Nat Nanotechnol* 12:194–206.
18. Xu W, et al. (2014) Lithium metal anodes for rechargeable batteries. *Energy Environ Sci* 7:513–537.
19. Aurbach D, Zinigrad E, Cohen Y, Teller H (2002) A short review of failure mechanisms of lithium metal and lithiated graphite anodes in liquid electrolyte solutions. *Solid State Ion* 148:405–416.
20. Bieker G, Winter M, Bieker P (2015) Electrochemical in situ investigations of SEI and dendrite formation on the lithium metal anode. *Phys Chem Chem Phys* 17:8670–8679.
21. Ji X, et al. (2012) Spatially heterogeneous carbon-fiber papers as surface dendrite-free current collectors for lithium deposition. *Nano Today* 7:10–20.
22. Stone GM, et al. (2012) Resolution of the modulus versus adhesion dilemma in solid polymer electrolytes for rechargeable lithium metal batteries. *J Electrochem Soc* 159: A222–A227.
23. Bouchet R, et al. (2013) Single-ion BAB triblock copolymers as highly efficient electrolytes for lithium-metal batteries. *Nat Mater* 12:452–457.
24. Yang C-P, Yin Y-X, Zhang S-F, Li N-W, Guo Y-G (2015) Accommodating lithium into 3D current collectors with a submicron skeleton towards long-life lithium metal anodes. *Nat Commun* 6:8058.
25. Lin D, Zhuo D, Liu Y, Cui Y (2016) All-integrated bifunctional separator for Li dendrite detection via novel solution synthesis of a thermostable polyimide separator. *J Am Chem Soc* 138:11044–11050.
26. Qian J, et al. (2015) High rate and stable cycling of lithium metal anode. *Nat Commun* 6:6362.
27. Li W, et al. (2015) The synergistic effect of lithium polysulfide and lithium nitrate to prevent lithium dendrite growth. *Nat Commun* 6:7436.
28. Bates JB, Dudney NJ, Neudecker B, Ueda A, Evans CD (2000) Thin-film lithium and lithium-ion batteries. *Solid State Ion* 135:33–45.
29. Murugan R, Thangadurai V, Weppner W (2007) Fast lithium ion conduction in garnet-type $\text{Li}_2\text{La}_3\text{Zr}_2\text{O}_{12}$. *Angew Chem Int Ed Engl* 46:7778–7781.
30. Kamaya N, et al. (2011) A lithium superionic conductor. *Nat Mater* 10:682–686.
31. Buschmann H, et al. (2011) Structure and dynamics of the fast lithium ion conductor " $\text{Li}_2\text{La}_3\text{Zr}_2\text{O}_{12}$ ". *Phys Chem Chem Phys* 13:19378–19392.
32. Lin D, et al. (2016) High ionic conductivity of composite solid polymer electrolyte via in situ synthesis of monodispersed SiO_2 nanospheres in poly (ethylene oxide). *Nano Lett* 16:459–465.
33. Choudhury S, Mangal R, Agrawal A, Archer LA (2015) A highly reversible room-temperature lithium metal battery based on crosslinked hairy nanoparticles. *Nat Commun* 6:10101.
34. Crowther O, West AC (2008) Effect of electrolyte composition on lithium dendrite growth. *J Electrochem Soc* 155:A806–A811.
35. Lin D, et al. (2016) Layered reduced graphene oxide with nanoscale interlayer gaps as a stable host for lithium metal anodes. *Nat Nanotechnol* 11:626–632.
36. Liu Y, et al. (2016) Lithium-coated polymeric matrix as a minimum volume-change and dendrite-free lithium metal anode. *Nat Commun* 7:10992.
37. Liang Z, et al. (2016) Composite lithium metal anode by melt infusion of lithium into a 3D conducting scaffold with lithophilic coating. *Proc Natl Acad Sci USA* 113: 2862–2867.
38. Xu K (2004) Nonaqueous liquid electrolytes for lithium-based rechargeable batteries. *Chem Rev* 104:4303–4417.
39. Xu K (2014) Electrolytes and interphases in Li-ion batteries and beyond. *Chem Rev* 114:11503–11618.
40. Ota H, Sakata Y, Wang X, Sasahara J, Yasukawa E (2004) Characterization of Lithium electrode in lithium imides/ethylene carbonate and cyclic ether electrolytes: II. Surface chemistry. *J Electrochem Soc* 151:A437–A446.
41. Aurbach D (2000) Review of selected electrode–solution interactions which determine the performance of Li and Li⁺ ion batteries. *J Power Sources* 89:206–218.
42. Yan K, et al. (2016) Selective deposition and stable encapsulation of lithium through heterogeneous seeded growth. *Nat Energy* 1:16010.
43. Zhao J, et al. (2014) Dry-air-stable lithium silicide-lithium oxide core-shell nanoparticles as high-capacity prelithiation reagents. *Nat Commun* 5:5088.
44. Sun Y, et al. (2016) High-capacity battery cathode prelithiation to offset initial lithium loss. *Nat Energy* 1:15008.
45. Sun Y, et al. (2016) In situ chemical synthesis of lithium fluoride/metal nanocomposite for high capacity prelithiation of cathodes. *Nano Lett* 16:1497–1501.
46. Zhao J, et al. (2016) Metallurgically lithiated SiO_2 anode with high capacity and ambient air compatibility. *Proc Natl Acad Sci USA* 113:7408–7413.
47. Chou C-Y, Kim H, Hwang GS (2011) A comparative first-principles study of the structure, energetics, and properties of Li–M (M = Si, Ge, Sn) Alloys. *J Phys Chem C* 115:20018–20026.
48. Aurbach D, Youngman O, Gofer Y, Meitav A (1990) The electrochemical behaviour of 1,3-dioxolane-LiClO₄ solutions. I. Uncontaminated solutions. *Electrochim Acta* 35: 625–638.
49. Ji X, Lee KT, Nazar LF (2009) A highly ordered nanostructured carbon-sulphur cathode for lithium-sulphur batteries. *Nat Mater* 8:500–506.
50. Busche MR, et al. (2014) Systematical electrochemical study on the parasitic shuttle-effect in lithium-sulfur-cells at different temperatures and different rates. *J Power Sources* 259:289–299.